Inorganic Chemistry

Article

pubs.acs.org/IC

Neutral, Cationic, and Anionic Low-Spin Iron(III) Complexes Stabilized by Amidophenolate and Iminobenzosemiquinonate Radical in *N*,*N*,*O* Ligands

Amit Rajput,[†] Anuj K. Sharma,[†] Suman K. Barman,[†] Debasis Koley,[§] Markus Steinert,[‡] and Rabindranath Mukherjee*,[†,§]

[†]Department of Chemistry, Indian Institute of Technology Kanpur, Kanpur 208 016, India

[‡]Institut für Anorganische Chemie, Georg-August-Universität Göttingen, Tammannstrasse 4, D-37077 Göttingen, Germany

[§]Department of Chemistry, Indian Institute of Science Education and Research Kolkata, Mohanpur Campus, Mohanpur 741 252, India

Supporting Information

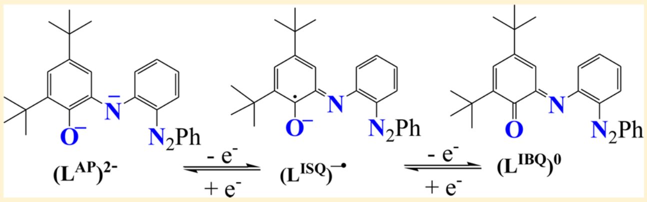

ABSTRACT: A brownish-black complex $[Fe^{III}(L)_2]$ (**1**) (S = 0), supported by two tridentate redox-active azo-appended *o*-amidophenolates [H_2L = 2-(2-phenylazo)-anilino-4,6-di-*tert*-butylphenol], has been synthesized and structurally characterized. In CH_2Cl_2 **1** displays two oxidative and two reductive $1e^-$ redox processes at $E_{1/2}$ values of 0.48 and 1.06 V and −0.42 and −1.48 V vs SCE, respectively. The one-electron oxidized form $[\mathbf{1}]^+$ isolated as a green solid $[Fe^{III}(L)_2][BF_4]$ (**2**) (S = 1/2) has been structurally characterized. Isolation of a dark ink-blue one-electron reduced form $[\mathbf{1}]^-$ has also been achieved $[Co^{III}(\eta^5\text{-}C_{10}H_{15})_2][Fe^{III}(L)_2]$ (**3**) (S = 1/2). Mössbauer spectral parameters unequivocally establish that **1** is a low-spin (LS) Fe^{III} complex. Careful analysis of Mössbauer spectral data of **2** and **3** at 200 and 80 K reveal that each complex has a major LS Fe^{III} and a minor LS Fe^{II} component (redox isomers): $[Fe^{III}\{(L^{ISQ})^{-\bullet}\}_2]^+$ and $[Fe^{II}\{(L^{IBQ})^0\}\{(L^{ISQ})^{-\bullet}\}]^+$ (**2**) and $[Fe^{III}\{(L^{AP})^{2-}\}_2]^-$ and $[Fe^{II}\{(L^{ISQ})^{-\bullet}\}\{(L^{AP})^{2-}\}]^-$ (**3**). Notably, for both at 8 K mainly the major component exists. Broken-Symmetry (BS) Density Functional Theory (DFT) calculations at the B3LYP level reveals that in **1** the unpaired electron of LS Fe^{III} is strongly antiferromagnetically coupled with a π-radical of *o*-iminobenzosemiquinonate(1−) $(L^{ISQ})^{-\bullet}$ form of the ligand, delocalized over two ligands providing 3− charge (X-ray structure). DFT calculations reveal that the unpaired electron in **2** is due to $(L^{ISQ})^{-\bullet}$ [LS Fe^{III} (S_{Fe} = 1/2) is strongly antiferromagnetically coupled to one of the $(L^{ISQ})^{-\bullet}$ radicals (S_{rad} = 1/2)] and **3** is primarily a LS Fe^{III} complex, supported by two *o*-amidophenolate(2−) ligands. Time-Dependent-DFT calculations shed light on the origin of UV−vis−NIR spectral absorptions for **1**−**3**. The collective consideration of Mössbauer, variable-temperature (77−298 K) electron paramagnetic resonance (EPR), and absorption spectral behavior at 298 K, and DFT results reveals that in **2** and **3** the valence-tautomerism is operative in the temperature range 80−300 K.

■ INTRODUCTION

Transition-metal complexes of redox-active ligands have long been recognized in coordination chemistry.[1] Because of redox-active character these ligands profoundly influence the electronic structural properties of the resulting complexes.[2] Notably, synergistic metal- and organic radical-based redox processes participate in enzymatic multielectron redox reactions.[3,4] Transition-metal complexes with redox-active ligands have generated much interest in recent years owing to an increased curiosity about the prospective role of various ligand-based oxidation levels and in catalysis.[4,5] Among a variety of redox-active ligand platforms[6−14] *o*-amidophenolates[1c,14] occupy a unique place via their observed coordination chemistry and spectroelectrochemical properties.

As a part of our interest in metal-coordinated radicals,[15] we have synthesized a new potentially tridentate *o*-aminophenol ligand which carries an additional redox-active azo group, 2-(2-phenylazo)-anilino-4,6-di-*tert*-butylphenol $H_2(L^{AP})$ (Figure 1). This ligand is unique in the sense that electron-rich *o*-amidophenolate(2−) unit will donate electron-density to the metal-ion but a π-accepting azo group is expected to withdraw electron-density to impart highly delocalized metal−ligand interaction. It is a generally accepted notion that the electron delocalization always reduces the molecular total energy and hence stabilizes a molecule.[16] In a molecule, a set of overlapping delocalized electronic states across the entire molecule is necessary for electronic conduction and hence such systems have the potential to function as molecular electronic devices.[17,18] Moreover, recent works on donor−acceptor properties[19] utilizing metal complexes with both kinds of ligands in a given complex—the *o*-amidophenolates[14] on one hand to act as donors and 2-(phenylazo)pyridines[13] on the other hand to act as acceptors, due to its azo function—have

Received: April 1, 2013
Published: December 10, 2013

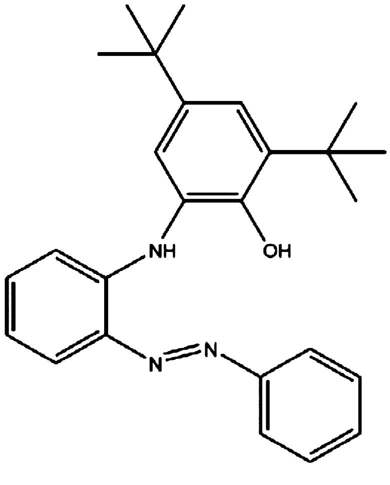

Figure 1. Structure of H_2L.

given an additional impetus to design our new ligand system and to explore the electronic structural properties of the resulting complexes. The works of Goswami[13c] and Verani[17b] deserve special mention with regard to the viability of molecular electronics, based on radical-containing coordination complexes. The net metal—ligand interaction is expected to be interesting and hence worthy of investigation. From this background we report here on the synthesis, structural characterization, and investigation of electronic structural properties, through a series of spectroscopic techniques, of an interesting new complex $[Fe^{III}(L)_2]$ (**1**), with two ligands providing 3− charge. As the ligand is expected to be redox-active we investigated the redox properties of **1**. We also describe the synthesis and characterization, including electronic structural aspects, of the monocation $[\mathbf{1}]^+$ and the monoanion $[\mathbf{1}]^-$ forms, in the successful synthesis of $[Fe^{III}(L)_2][BF_4]$ (**2**) and $[Co^{III}(\eta^5\text{-}C_{10}H_{15})_2][Fe^{III}(L)_2]$ (**3**), respectively. We report here also the structural properties of **2**. Results of Density Functional Theory (DFT) calculations at the B3LYP level of theory have been utilized to assign the correct oxidation level of the metal ion and also the coordinated ligands. Such results are presented here, along with the results of Time-Dependent (TD)-DFT calculations to throw light on the origin of UV—vis—NIR spectral absorptions for all the three complexes.

■ EXPERIMENTAL SECTION

General Considerations. All reagents were obtained from commercial sources and used as received. Solvents were dried/purified as reported previously.[20] 2-(Phenylazo)aniline[21] and $[Fe^{III}(acac)_3]$[22] ($acac^-$ = 2,4-pentanedione anion) were synthesized following reported procedures. Tetra-*n*-butylammonium perchlorate (TBAP) was prepared and purified as before.[23]

Synthesis of *H_2L*. To a stirring solution of 3,5-di-*tert*-butylcatechol (0.2 g, 0.9 mmol) in *n*-heptane (1 mL) was added Et_3N (0.12 mL) and a solution of 2-(phenylazo)aniline (0.177 g, 0.9 mmol) in *n*-heptane (1 mL), under a dinitrogen atmosphere. The reaction mixture was heated to reflux for 6 h, followed by stirring for 12 h. Solvent was then removed under reduced pressure, and the crude solid thus obtained was purified by silica-gel column chromatography. The dark red band that eluted first [ethylacetate: *n*-hexane, 5:95 (v/v)] was collected. Solvent removal afforded pure ligand as a dark red solid. Yield: 0.155 g, 43%. ^1H NMR ($CDCl_3$, 500 MHz): δ (ppm) 7.93 (d, J = 6.40 Hz, 2H; Ph-H_6), 7.88 (d, J = 7.35 Hz, 4H; Ph-H_7), 7.50 (t, J = 0.60 Hz, 4H; Ph-H_8), 7.44 (t, J = 0.25 Hz, 2H; Ph-H_9), 7.09 (s, 2H; Ph-H_1), 6.92 (t, J = 0.50 Hz, Ph-H_4 and Ph-H_5), 6.65 (d, J = 8.25 Hz, 2H; Ph-H_3), 6.15 (s, 2H; Ph-H_2), 1.46 (s, 9H; *tert*-butyl), 1.28 (s, 9H; *tert*-butyl). Positive ESI-MS 402.25 (100% peak M^+ + 1 ion peak).

Synthesis of Complexes. *$[Fe^{III}(L)_2]$ (**1**).* To a suspension of H_2L (0.3 g, 0.748 mmol) in MeOH (20 mL) was added Et_3N (0.151 g, 1.496 mmol), and stirred for 5 min. Solid $[Fe^{III}(acac)_3]$ (0.132 g, 0.374 mmol) was then added, and the reaction mixture was refluxed for 8 h. After cooling the dark precipitate that formed was filtered, washed with MeOH, and dried in vacuum. Yield: 0.298 g, ~47%. The crude solid was redissolved in CH_2Cl_2-MeOH (15 mL; 4:1 v/v) and left for slow evaporation, affording needles suitable for X-ray diffraction studies. Anal. Calcd for $C_{52}H_{58}N_6O_2Fe$ (**1**): C, 73.06; H, 6.84; N, 9.83. Found: C, 72.96; H, 6.74; N, 9.77. ^1H NMR ($CDCl_3$, 500 MHz): δ (ppm) 8.14 (d, J = 7.90 Hz, 4H; Ph-H_7), 7.97 (s, 2H; Ph-H_1), 7.08 (s, 2H; Ph-H_2), 6.86 (t, J = 0.35 Hz, 8H; Ph-H_4 and Ph-H_5), 6.63 (t, J = 0.25 Hz, 6H; Ph-H_8 and Ph-H_9), 1.56 (s, 9H; *tert*-butyl), 1.33 (s, 9H; *tert*-butyl).

*$[Fe^{III}(L)_2][BF_4]$ (**2**).* To a solution of $[Fe^{III}(L)_2]$ (0.1 g, 0.117 mmol) in CH_2Cl_2 (10 mL), solid $AgBF_4$ (0.023 g, 0.117 mmol) was added. The mixture was stirred at 298 K for 10 min and filtered (removal of metallic Ag). Solvent was then removed under reduced pressure, and the black solid thus formed was recrystallized from CH_2Cl_2-Et_2O (1:3, v/v). Black crystals that obtained were found to be suitable for X-ray structural study. Yield: 0.07 g, ~64%. Anal. Calcd for $C_{52}H_{58}N_6O_2FeBF_4$ (**2**): C 66.32, H 6.21, N 8.92. Found C 66.21, H 6.19, N 8.82. IR (KBr, cm^{-1}, selected peak): 1052 $\nu(BF_4^-)$.

*$[Co^{III}(\eta^5\text{-}C_{10}H_{15})_2]Fe^{III}(L)_2]$ (**3**).* To a solution of $[Fe^{III}(L)_2]$ (0.1 g, 0.117 mmol) in CH_2Cl_2 (10 mL), bis(pentamethylcyclopentadienyl)-cobalt(II) (0.039 g, 0.117 mmol) was added, under anaerobic conditions (Mbraun glovebox). The color of the solution immediately changed from black to ink-blue. After stirring for 4 h in the glovebox, the volume of the solution was reduced to ~2 mL, and dry degassed Et_2O (15 mL) was added with vigorous stirring. This resulted in the separation of a bluish-black solid, which was collected by filtration, washed with Et_2O, and dried in vacuum. Yield: 0.076 g, ~65%. Anal. Calcd for $C_{62}H_{68}N_6O_2FeCo$: C, 71.33; H, 6.56; N, 8.05. Found: C, 71.16; H, 6.49; N, 7.98.

Physical Measurements. Elemental analyses were obtained using Thermo Quest EA1110 CHNS-O, Italy. IR spectra (KBr, 4000—600 cm^{-1}) were recorded on a Bruker Vector 22 spectrophotometer. UV—vis spectra were recorded using an Agilent 8453 diode-array spectrophotometer. NIR absorption spectra were recorded using a JACSO V-670 (Japan) spectrophotometer. ^1H NMR spectra ($CDCl_3$) were obtained on a JEOL JNM LA 500 (500 MHz) spectrometer. Chemical shifts are reported in ppm referenced to TMS. ESI-MS spectra were recorded on a Waters-HAB213 spectrometer. X-band electron paramagnetic resonance (EPR) spectra were recorded by using either a Bruker EMX 1444 EPR spectrometer (fitted with a quartz Dewar for measurement at 77 K) operating at 9.455 GHz or a Magnettech GmbH MiniScope MS400 spectrometer (equipped with a temperature controller TC H03), where the microwave frequency was measured with a frequency counter FC400. The EPR spectra were calibrated with diphenylpicrylhydrazyl, DPPH (g = 2.0037). Spectra were treated by using the Bruker WinEPR software and simulated using the Bruker SIMFONIA software.

Cyclic voltammetric (CV) experiments were performed at 298 K by using CH instruments, Electrochemical Analyzer/Workstation model 600B series. The cell contained a Beckman M-39273 platinum-inlay working electrode, a Pt wire auxiliary electrode, and a saturated calomel electrode (SCE), as reference electrode. Details of the cell configuration are as described before.[23,24] For coulometry, a platinum wire-gauze was used as the working electrode. The solutions were ~1.0 mM in complex and 0.1 M in supporting electrolyte, TBAP. Spectroelectrochemical measurements were performed using a custom-made cell (Model EF-1350) from Bioanalytical Systems Inc., U.S.A.

Under our experimental conditions, the $E_{1/2}$ and peak-to-peak separation (ΔE_p) values in CH_2Cl_2 for $[Fe^{III}(\eta^5\text{-}C_5H_5)_2]^+/[Fe^{II}(\eta^5\text{-}C_5H_5)_2]$ (Fc^+/Fc) couple were 0.49 V vs SCE and 120 mV, respectively.[24]

Room-temperature magnetic susceptibility measurements were made on polycrystalline samples (powder form) of $[Fe^{III}(L)_2][BF_4]$ **2** and $[Co^{III}(\eta^5\text{-}C_{10}H_{15})_2][Fe^{III}(L)_2]$ (**3**) by the Faraday method using a locally built magnetometer.[25] Effective magnetic moment was calculated from $\mu_{eff} = 2.828[\chi_M T]^{1/2}$, where χ_M is the corrected molar susceptibility. The diamagnetic corrections were applied to the susceptibility data.[26] Solution-state magnetic susceptibilities were obtained by the NMR technique of Evans[27] in CH_2Cl_2 with a JEOL JNM LA 500 (500 MHz) spectrometer and made use of the paramagnetic shift of the methylene protons of CH_2Cl_2 as the measured NMR parameter.

^{57}Fe Mössbauer spectra at 298 K were recorded by using a Wissel 1200 spectrometer and a proportional counter. ^{57}Co(Rh) in a constant acceleration mode was used as the radioactive source. Temperature-dependent Mössbauer spectra were recorded with a conventional spectrometer with alternating constant acceleration of the source, either from Wissel or with a home-built setup (Georg-August-Universität Göttingen).[28]

Crystal Structure Determination. Single-crystals of suitable dimension were used for data collection. Diffraction intensities were collected on a Bruker SMART APEX CCD diffractometer, with graphite-monochromated Mo K_α ($\lambda = 0.71073$ Å) radiation at 100(2) K. The data were corrected for absorption. For **1**, out of 28 207 reflections measured, 10 647 were unique ($R_{int} = 0.0648$), and 6013 were used ($I > 2\sigma(I)$) for structure solution. The corresponding values for **2** are 52 888, 8148 (0.0813), and 6264. The structures were solved by SIR-97, expanded by Fourier-difference syntheses, and refined with the SHELXL-97 package incorporated in WinGX 1.64 crystallographic package.[29] The position of the hydrogen atoms were calculated by assuming ideal geometries, but not refined. All non-hydrogen atoms were refined with anisotropic thermal parameters by full-matrix least-squares procedures on F^2. Pertinent crystallographic parameters are summarized in Table 1.

Computational Details. All calculations were performed using the Gaussian 09 program.[30] Density Functional Theory (DFT) calculations employed the B3LYP functional[31] using all-electron Gaussian basis sets. The carbon and hydrogen were treated with split-valence plus polarization (SVP) basis sets of 6-31G* quality[32] and triple-ζ quality basis sets (TZVP) were used for iron, nitrogen, and oxygen.[33] The symmetry-broken,[34] singlet-diradical wave function of **1** was optimized in Gaussian 09.[30] Initially, the stability analysis of the restricted DFT wave function was performed using the "stable=opt" keyword. If any symmetry-broken DFT solution exists then the program automatically finds the lowest energy wave function. This is further verified by taking the restricted DFT wave function and performing optimization with "guess=mix" keyword. The symmetry-broken solution is measured from the expectation value of the spin operator ($\langle S^2 \rangle$), which is different from zero. For the monocation $[\mathbf{1}]^+$ the optimization was carried out starting from the X-ray structural coordinates of **1** with $S = 1/2$ and a positive charge. Then the stability analysis of the wave function leads to the broken-symmetry solution. Similarly, for the monoanion $[\mathbf{1}]^-$ the optimization was carried out starting from the X-ray coordinates of **1** with $S = 1/2$ and a negative charge. Stability analysis revealed that the wave function was already stable. Corresponding orbitals and spin-density plots were made using VMD[35a] and Chemcraft[35b] Visualization programs. The wave functions of optimized geometries (at B3LYP functional) for all the complexes were used in Time-Dependent (TD)-DFT calculations employing the BP86 functional and the polarizable continuum model, CPCM (CH_2Cl_2 as solvent).[36] TD-DFT-derived electronic spectra were plotted using GaussSum.[37]

Table 1. Data Collection and Structure Refinement Parameters for $[Fe^{III}(L)_2]$ 1 and $[Fe^{III}(L)_2][BF_4]$ 2

	1	2
empirical formula	$C_{52}H_{58}FeN_6O_2$	$C_{52}H_{58}FeN_6O_2BF_4$
formula weight	854.89	1005.99
crystal color, habit	black, prism	black, block
temperature (K)	100(2)	100(2)
wavelength (Å)	0.71073	0.71073
crystal system	orthorhombic	trigonal
space group	$Pca2_1$ (no. 29)	$R3c$ (no. 161)
crystal size (mm^3)	0.10 × 0.08 × 0.06	0.12 × 0.10 × 0.08
a (Å)	22.475(3)	30.9863(9)
b (Å)	12.0625(16)	30.9863(9)
c (Å)	16.508(2)	28.9032(16)
α (deg)	90.0	90.0
β (deg)	90.0	90.0
γ (deg)	90.0	120.0
volume (Å^3)	4475.4(10)	24033.4(17)
Z	4	18
density$_{calc}$ (g cm^{-3})	1.220	1.251
μ (mm^{-1})	0.385	0.348
no. reflcns collcd	28207	52888
no. unique reflcns	10647 ($R_{int} = 0.0648$)	8148 ($R_{int} = 0.0813$)
no. reflcns used [$I > 2\sigma(I)$]	6013	6264
goodness-of-fit on F^2	0.99	1.048
final R indices [$I > 2\sigma(I)$]^{a,b}	0.0682 (0.1303)	0.0857 (0.2255)
R indices (all data)^{a,b}	0.1601 (0.2124)	0.1135 (0.2573)

$^a R_1 = \sum||F_o| - |F_c||/\sum|F_o|$. $^b wR_2 = \{\sum[w(|F_o|^2 - |F_c|^2)^2]/\sum[w(|F_o|^2)^2]\}^{1/2}$.

■ RESULTS AND DISCUSSION

Synthesis of a New Ligand H_2L and $[Fe^{III}(L)_2]$ 1. The ligand H_2L was synthesized by stoichiometric reaction between 3,5-di-*tert*-butylcatechol and 2-(phenylazo)aniline in *n*-heptane in the presence of Et_3N, under a dinitrogen atmosphere. Purification was achieved by silica-gel column chromatography, affording a dark red solid. Purity was checked by its ^{1}H NMR (Figure S1, Supporting Information) and ESI-MS spectra. Wieghardt and co-workers[9,38] unequivocally established that *o*-amidophenolates are redox-active *O,N*-coordinated ligands which can exist in different protonation and oxidation levels in coordination compounds. Other groups have provided examples to strengthen this trend.[39−41] The expected redox behavior of $(L^{AP})^{2-}$ from both *o*-amidophenolate and azo functionality is shown in Scheme 1.

Aerobic reaction of $[Fe^{III}(acac)_3]$ with H_2L and Et_3N in MeOH under refluxing conditions afforded, after work up and recrystallization from CH_2Cl_2-MeOH, X-ray quality black crystals of $[Fe^{III}(L)_2]$ **1**. Complex **1** exhibits in $CDCl_3$ a clean ^{1}H NMR spectrum in the δ 0−10 ppm range, attesting to its diamagnetic character (Figure S2, Supporting Information). Positive ESI-MS of **1** in CH_2Cl_2 showed a peak at $m/z = 855.4$ corresponding to the species $\{[Fe^{III}(L)_2] + [H]^+\}$, based on the simulated mass and isotopic distribution pattern (Figure S3, Supporting Information).

Redox Properties of 1. To investigate the possibility of identifying metal-centered redox and/or accessibility of various ligand redox levels, cyclic voltammetry (CV) experiments on **1** were carried out. The CV of **1** in CH_2Cl_2 solution displays (Figure 2) four redox processes: two reductions at $E_{1/2}$ values of −0.42 V (peak-to-peak separation, ΔE_p = 180 mV) and −1.48 V (ΔE_p = 240 mV) and two oxidations at $E_{1/2}$ values of 0.48 V (ΔE_p = 160 mV) and 1.06 V (ΔE_p = 300 mV) vs SCE. Both the first oxidation and the first reduction processes are chemically reversible (ratio of cathodic and anodic peak current, $i_{pc}/i_{pa} \approx 1$)[24] and electrochemically quasireversible electron-transfer reactions. The most cathodic and most anodic redox processes were not investigated any further.

Scheme 1

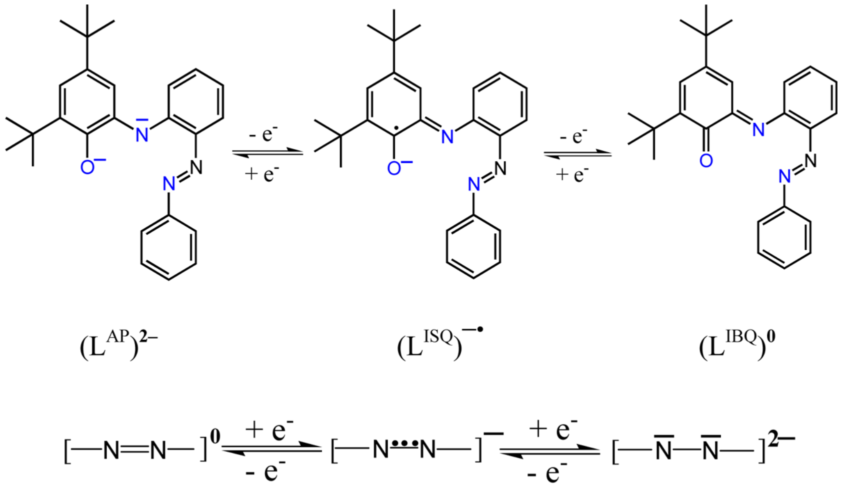

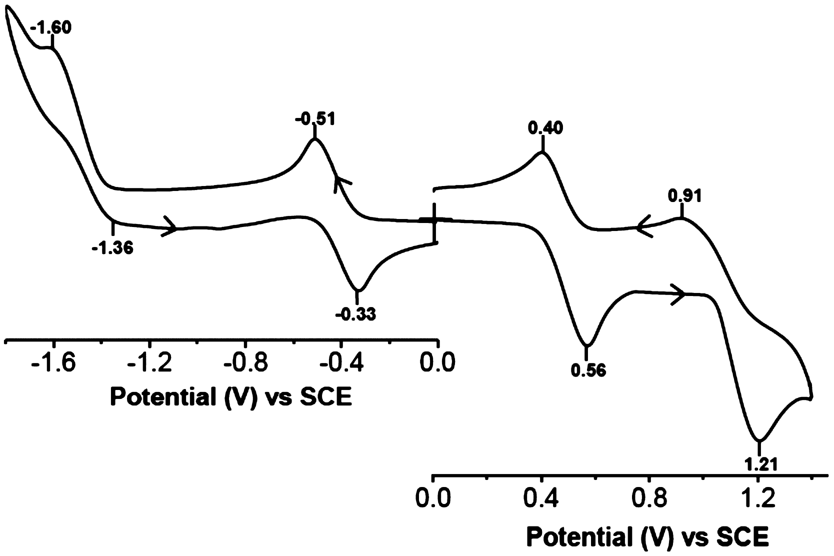

Figure 2. Cyclic voltammogram (100 mV/s) of a 1.0 mM solution of $[Fe^{III}(L)_2]$ **1** in CH_2Cl_2 (0.1 M in TBAP) at a platinum working electrode. Indicated peak potentials are in V vs SCE.

Synthesis and Characterization of $[Fe^{III}(L)_2][BF_4]$ 2 and $[Co^{III}((\eta^5\text{-}C_{10}H_{15})_2][Fe^{III}(L)_2]$ 3. Coulometric oxidation of **1** in CH_2Cl_2 (0.1 M TBAP; 298 K) at 0.7 V vs SCE established that the wave at $E_{1/2}$ = 0.48 V corresponds to a one-electron process. The oxidized form $[\mathbf{1}]^+$ was found to be stable on the time scale of CV (Figure S4, Supporting Information). In fact, this behavior finally led to designed chemical synthesis of **2**. Controlled-potential coulometry of **1** in CH_2Cl_2 (0.1 M TBAP; 298 K) at −0.7 V vs SCE established that the wave at −0.42 V corresponds to a one-electron reduction process, yielding $[\mathbf{1}]^-$. The reduced form of **1** was found to be stable under anaerobic conditions, which finally led to designed chemical synthesis of **3**. Electrochemical reoxidation of such solutions (Figure S5, Supporting Information) produced quantitatively the starting complex **1**.

Clean one-electron chemical oxidation of **1** in CH_2Cl_2 at 298 K by 1 equiv of $AgBF_4$[42] was achieved. Solvent removal afforded a solid, which on usual workup led to the isolation of a greenish-black solid $[Fe^{III}(L)_2][BF_4]$ **2**. Chemical reduction of **1** could be achieved in CH_2Cl_2 at 298 K by 1 equiv of bis(pentamethylcyclopentadienide)cobalt(II) $[Co^{II}(\eta^5\text{-}C_{10}H_{15})_2]$,[43,44] under anaerobic conditions. Usual workup of this solution produced ink-blue air-sensitive microcrystals of $[Co^{III}(\eta^5\text{-}C_{10}H_{15})_2][Fe^{III}(L)_2]$ (**3**).

The absence of ν(O−H) and ν(N−H) in the IR spectra of **1**−**3** confirmed that the ligand is coordinated in these complexes in the doubly deprotonated form. Elemental analyses and IR data are in agreement with the above formulations. Effective magnetic moment (μ_{eff}) values of solid samples of **2** and **3** measured at 298 K were determined to be 1.89 μ_B and 1.91 μ_B, respectively. Solution-state values of coulometrically generated one-electron oxidized $[\mathbf{1}]^+$ and one-electron reduced $[\mathbf{1}]^-$ forms were calculated to be 1.91 μ_B and 1.84 μ_B, respectively. Thus $[\mathbf{1}]^+$/**2** and $[\mathbf{1}]^-$/**3** are paramagnetic with respect to one unpaired electron. The stability of **2** and **3** in CH_2Cl_2 solutions was investigated by their clean ESI-MS pattern. Positive and negative ESI-MS of **2** (Figure S6, Supporting Information) displayed peaks at m/z = 854.40 and 87, respectively. Based on the simulated mass and isotopic distribution pattern these peaks correspond to the species $[Fe^{III}(L)_2]^+$ and $[BF_4]^-$, respectively. Positive and negative ESI-MS of **3** (Figure S7, Supporting Information) showed peaks at

Table 2. Selected Bond Lengths (Å) and Bond Angles (deg) in $[Fe^{III}(L)_2]$ 1 and $[Fe^{III}(L)_2][BF_4]$ 2

1		2	
Fe−N1	1.896(4)	Fe−N1	1.889(6)
Fe−N3	1.927(4)	Fe−N3	1.923(6)
Fe−O1	1.957(3)	Fe−O1	1.955(5)
O1−C26	1.315(6)	O1−C26	1.278(9)
C13−C26	1.426(7)	C13−C26	1.436(10)
C13−C14	1.397(7)	C13−C14	1.414(10)
C14−C15	1.404(7)	C14−C15	1.360(11)
C15−C20	1.401(8)	C15−C20	1.412(10)
C20−C21	1.387(7)	C20−C21	1.368(11)
C21−C26	1.440(7)	C21−C26	1.453(10)
N1−C12	1.368(6)	N1−C12	1.381(11)
N1−C13	1.402(6)	N1−C13	1.366(9)
C7−C12	1.433(7)	C7−C12	1.405(11)
C7−C8	1.422(7)	C7−C8	1.421(10)
C8−C9	1.366(8)	C8−C9	1.397(13)
C9−C10	1.377(9)	C9−C10	1.376(13)
C10−C11	1.384(8)	C10−C11	1.368(11)
C11−C12	1.394(7)	C11−C12	1.406(11)
N2−C7	1.378(7)	N2−C7	1.395(10)
N2−N3	1.280(6)	N2−N3	1.271(8)
N3−C6	1.454(7)	N3−C6	1.465(9)
C6−C1	1.379(8)	C6−C1	1.377(11)
C1−C2	1.372(9)	C1−C2	1.370(12)
C2−C3	1.372(10)	C2−C3	1.385(14)
C3−C4	1.376(10)	C3−C4	1.429(15)
C4−C5	1.397(8)	C4−C5	1.386(12)
C5−C6	1.390(8)	C5−C6	1.379(11)
Fe−N4	1.886(4)	Fe−N4	1.880(6)
Fe−N6	1.928(4)	Fe−N6	1.927(6)
Fe−O2	1.955(3)	Fe−O2	1.929(5)
O2−C52	1.307(6)	O2−C52	1.302(9)
C52−C39	1.430(7)	C52−C39	1.441(10)
C39−C40	1.404(7)	C39−C40	1.394(10)
C40−C41	1.383(7)	C40−C41	1.377(10)
C41−C46	1.419(9)	C41−C46	1.447(10)
C46−C47	1.381(8)	C46−C47	1.338(10)
C47−C52	1.439(7)	C47−C52	1.428(10)
N4−C39	1.364(6)	N4−C39	1.368(9)
N4−C38	1.379(6)	N4−C38	1.389(9)
C33−C38	1.436(7)	C33−C38	1.396(10)
C33−C34	1.419(8)	C33−C34	1.424(10)
C34−C35	1.353(8)	C34−C35	1.378(12)
C35−C36	1.387(9)	C35−C36	1.388(11)
C36−C37	1.376(8)	C36−C37	1.374(10)
C37−C38	1.418(7)	C37−C38	1.409(10)
N5−C33	1.379(7)	N5−C33	1.374(10)
N5−N6	1.283(6)	N5−N6	1.267(8)
N6−C32	1.451(7)	N6−C32	1.449(9)
C27−C32	1.378(8)	C27−C32	1.388(10)
C27−C28	1.408(9)	C27−C28	1.353(12)
C28−C29	1.363(11)	C28−C29	1.409(14)
C29−C30	1.375(11)	C29−C30	1.381(14)
C30−C31	1.394(9)	C30−C31	1.366(12)
C31−C32	1.382(8)	C31−C32	1.384(11)
Fe−N1−C13	109.8(3)	Fe−N1−C13	110.3(4)
Fe−N1−C12	125.8(3)	Fe−N1−C12	125.7(5)
C12−N1−C13	124.4(3)	C12−N1−C13	124.0(6)
N1−Fe−N3	90.73(19)	N1−Fe−N3	89.9(2)
N1−Fe−N4	169.33(17)	N1−Fe−N4	170.5(2)
N1−Fe−N6	96.21(18)	N1−Fe−N6	96.5(3)
N3−Fe−N6	92.96(18)	N3−Fe−N6	92.4(2)
N3−Fe−N4	96.59(18)	N3−Fe−N4	96.1(3)
N4−Fe−N6	91.18(18)	N4−Fe−N6	90.6(2)
N2 -N3—Fe	128.7(4)	N2 −N3-Fe	129.6(5)
N5 -N6—Fe	128.6(3)	N5 −N6-Fe	128.6(5)
Fe−N4−C38	125.3(3)	Fe−N4−C38	123.8(5)
Fe−N4−C39	109.9(3)	Fe−N4−C39	110.9(4)
C38−N4−C39	124.7(4)	C38−N4−C39	125.2(6)
N1−Fe−O1	83.87(16)	N1−Fe−O1	82.9(2)
N1−Fe−O2	88.30(16)	N1−Fe−O2	89.1(2)
N3−Fe−O1	173.17(17)	N3−Fe−O1	171.9(2)
N3−Fe−O2	90.72(17)	N3−Fe−O2	92.8(2)
N4−Fe−O1	88.22(16)	N4−Fe−O1	90.6(2)
N4−Fe−O2	83.86(16)	N4−Fe−O2	83.3(2)
N6−Fe−O1	91.78(17)	N6−Fe−O1	91.9(2)
N6−Fe−O2	174.13(17)	N6−Fe−O2	172.3(2)
O1−Fe−O2	84.96(15)	O1−Fe−O2	83.58(19)

m/z = 329.17 and 854.40, respectively. Simulated mass and isotopic distribution pattern of these peaks correspond to the species $[Co^{III}(\eta^5\text{-}C_{10}H_{15})_2]^+$ and $[Fe^{III}(L)_2]^-$, respectively.

Complexes **1** and **2** have been structurally characterized (see Crystal Structure section). In spite of our sincere efforts so far we have not succeeded in growing single-crystals of **3** suitable for crystallographic studies.

Description of the Structures. To confirm the structure of the complexes and to extract information on the oxidation level of both iron and coordinated ligands single-crystal X-ray structure determination of the parent complex $[Fe^{III}(L)_2]$ **1** and its one-electron oxidized counterpart $[Fe^{III}(L)_2][BF_4]$ **2** were carried out. Selected bond length and bond angles are listed in Table 2.

$[Fe^{III}(L)_2]$ 1. A perspective view of the metal coordination environment in **1** is shown in Figure 3. Given the neutral nature of **1**, both the tridentate ligands can exist either as a one-electron paramagnetic *o*-iminobenzosemiquinonate(1−) π radical $(L^{ISQ})^{-\bullet}$ coordinated to Fe^{II} ion or as a combination of both diamagnetic dianionic *o*-amidophenolate $(L^{AP})^{2-}$ and paramagnetic $(L^{ISQ})^{-\bullet}$ coordinated to Fe^{III} ion.

o-Amidophenolates(2−) are redox-active and can exist in three redox levels, and Scheme 1 shows the geometric features observed. Wieghardt and others[1c,9,14,38−42] firmly established that it is possible to unambiguously discern these forms in a complex by high-quality X-ray crystallography, if the estimated experimental error of the C−C, C−O, and C−N bond lengths is not larger than 0.015 Å (3σ). For $(L^{AP})^{2-}$ the C−O and C−N bonds are ~1.35 Å and ~1.37 Å, respectively. For $(L^{ISQ})^{-\bullet}$, where the six-membered ring is not equivalent (quinoid-type distortion) comprising a short, a long, and another short C−C bond followed by three long ones and, in addition, both the C−O and C−N distances are significantly shorter (~1.30 and ~1.35 Å, respectively) than those in $(L^{AP})^{2-}$. The trend observed for $(L^{ISQ})^{-\bullet}$ is further amplified upon oxidation by one more electron to the $(L^{IBQ})^0$ level, with C−O and C−N bond distances of ~1.24 and ~1.30 Å, respectively.

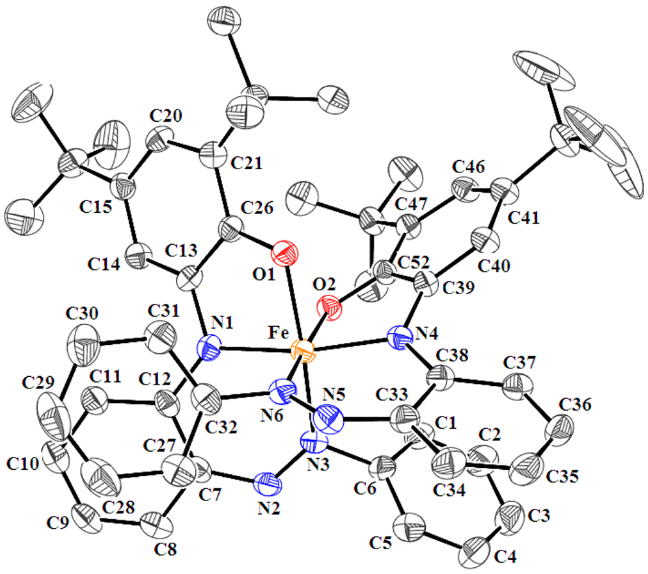

Figure 3. Perspective view of $[\mathrm{Fe^{III}(L)_2}]$ **1**.

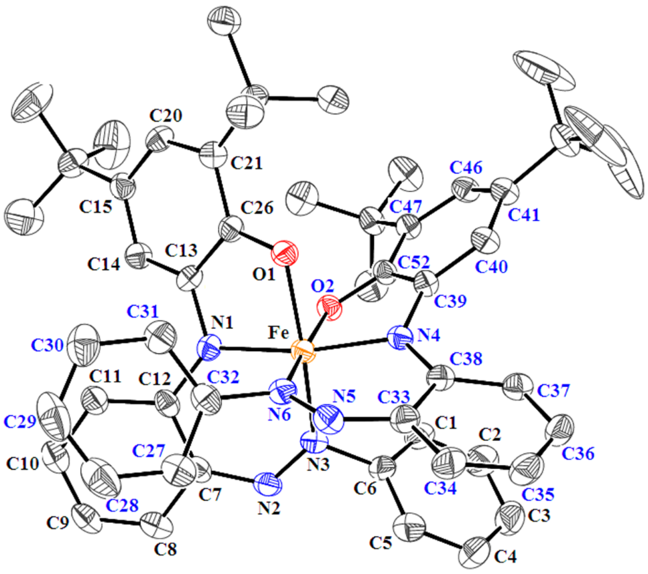

Figure 4. Perspective view of $[\mathrm{Fe^{III}(L)_2}][\mathrm{BF_4}]$ **2**.

The sensitive C−O, C−N, and intraring bond distances associated with the coordinated ligands in **1** (Table 2) reveal the following important features. (i) The C−O and C−N bond distances exhibit a rather complex relationship where the C−O distances [1.307(6) and 1.315(6) Å] are closer to the localized $(\mathrm{L^{ISQ}})^{-\bullet}$ distance, whereas the C−N distance of one ligand 1.364(6) Å is in between the distances for localized $(\mathrm{L^{AP}})^{2-}$ and $(\mathrm{L^{ISQ}})^{-\bullet}$ forms and for the other ligand the distance 1.402(6) is larger than even the localized $(\mathrm{L^{AP}})^{2-}$ form. Given the set benchmark by Wieghardt and others,[1c,9,14,38−42] the observed metric parameters and the accuracy level of observed bond lengths (3σ value: ± 0.021 for C−C, ± 0.018 for both C−O and C−N), it is not possible to unambiguously assign the oxidation level of the coordinated ligands in **1**. The observed parameters, however, suggest that two ligands provide 3− charge and a radical is delocalized over two ligands.[41a] Admittedly, it is not exact, but it is a reasonable approximation that one ligand is in the $(\mathrm{L^{AP}})^{2-}$ form and the other in the *o*-iminobenzosemiquinonate(1−) π radical $(\mathrm{L^{ISQ}})^{-\bullet}$ form. The Fe atom must then be ascribed a +3 oxidation state. The observed Fe−O [Fe−O1 1.957(3) and 1.955(3) Å] and Fe−N [Fe−N1 1.896(4) and 1.886(4) Å] bond distances support this view with iron in the low-spin (LS) state (see Mössbauer section). The Fe−N(azo) distances are the longest [Fe−N3 1.927(4) and Fe−N6 1.928(4) Å], revealing that azo group has not pulled much electron density, meaning thereby not significant resonance delocalization in the azo part of the present ligand (N−N bond distances N2−N3 1.280(6) and N5−N6 1.283(6) Å). The N−N distance is an excellent indicator of the charge on an azo function. From ∼1.24 Å for free ligands the coordination by back-donating metals may shift this value to about 1.25−1.30 Å. Authentic one-electron reduced (i.e., anion radical) ligands have N−N distance of ∼1.35 Å.[41b,45,46] It is worth mentioning here that in high-spin tris-complex of bidentate 2-anilino-4,6-di-*tert*-butylphenolate in which the ligands are in the $(\mathrm{L^{ISQ}})^{-\bullet}$ oxidation level, the distances are Fe−O 2.015(3), 2.018(3), and 2.009(3) Å and Fe−N 2.057(4), 2.149(4), and 2.091(4) Å.[38b]

$[\mathrm{Fe^{III}(L)_2}][\mathrm{BF_4}]$ 2. A perspective view of the metal coordination environment in **2** is shown in Figure 4. The C−O and C−N bond distances for one ligand are 1.278(9) and 1.366(9) Å, respectively. For the other ligand, the corresponding distances are 1.302(9) Å and 1.368(9) Å, respectively. As that observed for **1**, the C−O and C−N bond distances do not fall under the set benchmark: (i) the C−O distance of one ligand is shorter than localized $(\mathrm{L^{ISQ}})^{-\bullet}$ and for the other it is closer to the localized $(\mathrm{L^{ISQ}})^{-\bullet}$ distance. (ii) The C−N distance of both the ligands corresponds to either the localized $(\mathrm{L^{AP}})^{2-}$ or the localized $(\mathrm{L^{ISQ}})^{-\bullet}$ form. Clearly, the behavior can be attributed to the effect of delocalization of metal and ligand.[41a] The accuracy level of bond length determination (3σ values: ± 0.030 Å for C−C and ±0.027 Å for both C−O and C−N bonds) and hence the observed metric parameters (Table 2) do not allow us to unambiguously assign the oxidation level of the coordinated ligands in **2**. However, the composition and observed metric parameters of this monocation suggest that two ligands provide together 2− charge, and each is present in the *o*-iminobenzosemiquinonate(1−) π radical $(\mathrm{L^{ISQ}})^{-\bullet}$ form (Scheme 1). Understandably, it is a reasonable approximation. The observed Fe−O and Fe−N bond distances are Fe−O1 1.955(5) and 1.929(5) Å and Fe−N1 1.889(6) and 1.880(6) Å. The Fe−N(azo) distances are Fe−N3 1.923(4) and Fe−N6 1.927(6) Å. The N−N bond distances are N2−N3 1.271(8) and N5−N6 1.267(8) Å, attesting that as in **1** not significant resonance delocalization is present in the azo part of the present ligand.

Mössbauer Spectra. The zero-field ^{57}Fe Mössbauer spectra of $[\mathrm{Fe^{III}(L)_2}]$ **1** were recorded at 298 and 200 K (Figure S8, Supporting Information), and 80 K displaying (Figure S9, Supporting Information) uniformly a symmetric quadrupole doublet. The parameters (Table 3) are in complete accord with the d^5 LS Fe$^{\mathrm{III}}$.[47] To elucidate the electronic structure of its one-electron oxidized $[\mathbf{1}]^+$ and one-electron reduced $[\mathbf{1}]^-$ forms we have recorded temperature-dependent Mössbauer spectra of **2** and **3**, respectively (Table 3).

The spectrum of **2** at 80 K could be satisfactorily fitted by two subspectra (Figure 5): an intense symmetric quadrupole doublet and a minor symmetric doublet. The relative intensity of the minor doublet increases at 200 K (Figure 5). At 8 K the minor doublet completely disappears (Figure S9, Supporting Information). The minor doublet could be due to either a LS Fe$^{\mathrm{II}}$ or a high-spin (HS) Fe$^{\mathrm{III}}$ (spin-state transition) species.

Table 3. Zero-Field Mössbauer Parameters[a,b] of $[Fe^{III}(L)_2]$ 1, $[Fe^{III}(L)_2][BF_4]$ 2, and $[Co^{III}(\eta^5\text{-}(C_{10}H_{15})_2][Fe^{III}(L)_2]$ 3

		LS Fe^{III}		LS Fe^{II}		
		A(1)		A(2)		
complex	*T*, K	δ, mms^{-1}	ΔE_Q, mms^{-1}	δ, mms^{-1}	ΔE_Q, mms^{-1}	relative intensity A(1):A(2), %
1	298	0.04	2.13			100
1	200	0.09	1.94			100
1	80	0.11	1.97			100
2	200	0.13	1.87	0.47	0.73	72:28
2	80	0.14	1.85	0.73	1.06	93:7
2	8	0.16	1.90			100
3	200	0.07	1.99	0.56	1.13	80:20
3	80	0.13	1.99	0.61	1.06	86:14
3	8	0.14	2.03			100
		0.14	2.03	0.63	1.05	96:4

[a] Isomer shift vs α-Fe at 20 °C. [b] Quadrupole splitting.

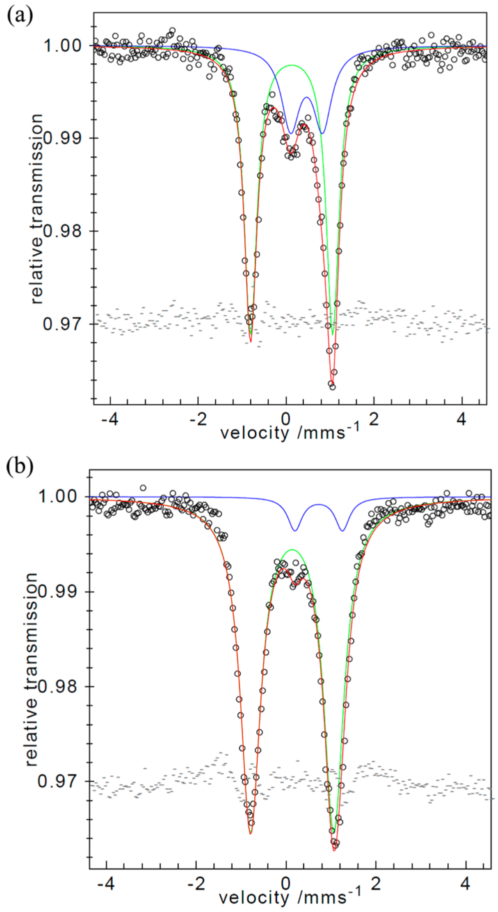

Figure 5. Zero-field ^{57}Fe Mössbauer spectra (solid) of $[Fe^{III}(L)_2][BF_4]$ **2** (a) at 200 K (fitting of two subspectra) and (b) 80 K (fitting of two subspectra).

Given the metal−ligand bonding parameters of LS Fe^{III} in **2** obtained at 100 K (Table 2), the spin-transition to HS Fe^{III} at 80 K is not feasible. On a similar ground and also given the spectral parameters we rule out the possibility of HS Fe^{II}. The LS Fe^{II} is definitely a possibility.[48,49] At 8 K, the spectrum of **2** is a pure LS Fe^{III} complex (Figure S9, Supporting Information). The data for **2** at 80 K could be fitted by three subspectra as well (Figure S10, Supporting Information): two symmetric quadrupole doublets $\delta = 0.13$ mm s^{-1}, $\Delta E_Q = 2.04$ mm s^{-1} (49% relative intensity) and $\delta = 0.14$ mm s^{-1}, $\Delta E_Q = 1.59$ mm s^{-1} (43% relative intensity), and a minor symmetric doublet at $\delta = 0.75$ mm s^{-1} and $\Delta E_Q = 1.13$ mm s^{-1} (8% relative intensity). Given the data at hand (see EPR section) we believe that two subspectra (Figure 5) represent the right fit for **2**.

The spectrum of **3** recorded at 80 K also point toward the presence of two species. The data could be satisfactorily fitted (Figure 6) by two subspectra: an intense symmetric quadrupole doublet and a minor symmetric doublet. The relative intensity of the minor doublet increases at 200 K (Figure 6), as that observed for **2**. Here also at 8 K the minor doublet completely

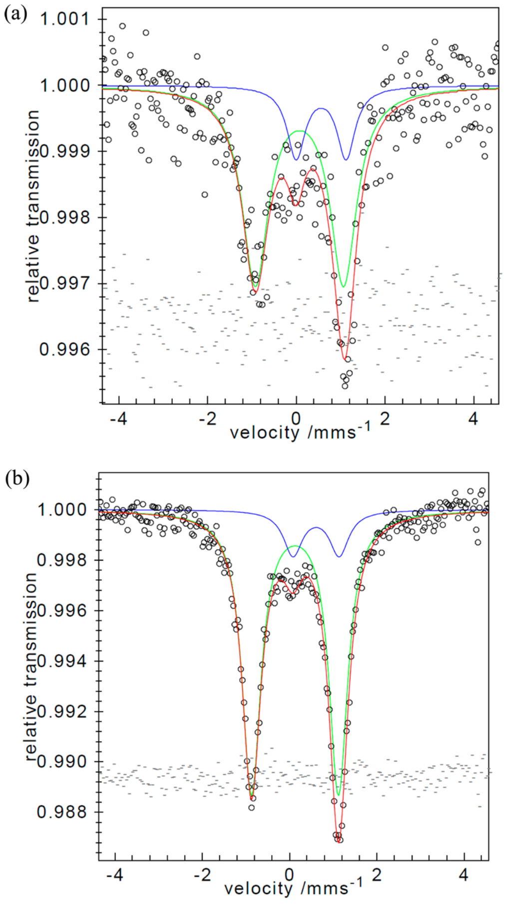

Figure 6. Zero-field ^{57}Fe Mössbauer spectrum (solid) of $[Co^{III}(\eta^5\text{-}C_{10}H_{15})_2][Fe^{III}(L)_2]$ **3** (a) at 200 K (fitting of two subspectra) and (b) 80 K (fitting of two-subspectra).

disappears (Figure S9, Supporting Information). Given the asymmetry of the spectrum at 8 K we fitted the data by two subspectra: an intense symmetric quadrupole doublet (Figure S11, Supporting Information) and a minor symmetric doublet (Table 3; see EPR section). Clearly, the quality of the fitting improves.

Temperature-dependent Mössbauer spectral behavior of **2** and **3** could be explained if we invoke the occurrence of thermally driven valence-tautomerism.[2b,c,7a,10−12,42,50,51] In the case of **2** we consider the equilibrium $[Fe^{III}\{(L^{ISQ})^{-\bullet}\}_2]^+$ (LS Fe^{III}) $\rightleftharpoons$ $[Fe^{II}\{(L^{IBQ})^o\}\{(L^{ISQ})^{-\bullet}\}]^+$ (LS Fe^{II}) in the solid state (see EPR section). In fact, the $Fe^{III}-(L^{ISQ})^{-\bullet} \rightleftharpoons Fe^{II}-(L^{IBQ})^0$ equilibrium is related by exchange of an electron between the metal ion and the coordinated redox-active ligand, keeping the total spin $S_t = 1/2$ invariant. We believe that this phenomenon is operative in the 80−200 K range. The presence of strong $Fe^{III}-(L^{ISQ})^{-\bullet}$ exchange interaction in **2** strengthens our hypothesis and rules out the possibility of the existence of another thermally driven valence-tautomer $[Fe^{III}\{(L^{AP})^{2-}\}\{(L^{IBQ})^0\}]^+$ (LS Fe^{III}), and hence three-subspectra fitting is discarded. For **3** we consider the equilibrium $[Fe^{III}\{(L^{AP})^{2-}\}_2]^-$ (LS Fe^{III}) $\rightleftharpoons$ $[Fe^{II}\{(L^{ISQ})^{-\bullet}\}\{(L^{AP})^{2-}\}]^-$ (LS Fe^{II}) in the solid state (see EPR section). Recent theoretical studies have concluded that owing to the energetic proximity of the metal d-orbitals and the frontier ligand orbitals of redox-active ligands, the transition-metal complexes of such ligands may exhibit thermally induced reversible valence-tautomeric behavior.[51] The temperature-dependent Mössbauer spectral behavior of **2** and **3** is thus understandable.

Absorption Spectra. Measurements were recorded in CH_2Cl_2 (Figure 7). For **3** the measurements were done strictly under anaerobic conditions. Bluish-black solutions of **1** display very intense (~10^4 M^{-1} cm^{-1}) absorptions at 420 nm (ε, 11 750 M^{-1} cm^{-1}), 490 (13 000), 540 (12 970), 685 (17 800), and 1590 (13 650). Greenish-black solutions of **2** display (Figure 7) intense (~10^3 M^{-1} cm^{-1}) absorptions at 435 (6500), 600 (5800), 860 sh (2700), 1010 sh (2600), 1130 (3000), 1580 sh (600), 1890 (1100). Ink-blue solutions of **3** display (Figure 7) very intense (~10^3 M^{-1} cm^{-1}) absorptions at 425 (6520), 570 (8900), 650 sh (8600), 755 sh (5480) 1060 (1910), 1590 (1600). The conversion of **1** to **3** is accompanied by the appearance of a new peak at 1060 nm. Moreover, the absorption band maxima in the 450−900 nm region are shifted, and the intensities are lowered. In going from **1** to **2** a new peak appears at 1890 nm, the absorption band maxima in the said region are shifted, and the intensities are further lowered. It is interesting to note that the absorption at ~1590 nm remains invariant in going from **1** to $[\mathbf{1}]^-$ or $[\mathbf{1}]^+$; however, the intensity of the absorption monotonically decreases. This observation does not corroborate well with the significant change in the electronic structure of the ligand(s). In fact, it correlates well with closely similar electronic structure. The existence of valence-tautomeric equilibria[2b,c,7a,10−12,42,50,51] $[Fe^{III}\{(L^{ISQ})^{-\bullet}\}_2]^+$ (LS Fe^{III}) $\rightleftharpoons$ $[Fe^{II}\{(L^{IBQ})^o\}\{(L^{ISQ})^{-\bullet}\}]^+$ (LS Fe^{II}) and $[Fe^{III}\{(L^{AP})^{2-}\}_2]^-$ (LS Fe^{III}) $\rightleftharpoons$ $[Fe^{II}\{(L^{ISQ})^{-\bullet}\}\{(L^{AP})^{2-}\}]^-$ (LS Fe^{II}) could explain the spectral behavior of **2** and **3**, respectively. Given the delocalized nature of the coordinated ligands (see X-ray structure and Mössbauer section) such a phenomenon is justifiable. The origin of observed absorptions for **1**, **2**, and **3** is described later (see TD-DFT section).

Spectroelectrochemistry. Experiments were done in CH_2Cl_2 (0.1 M TBAP) at 298 K, and the spectra were recorded in the 300−1000 nm region. Figure 8a shows the changes in the absorption spectral feature during electrochemical oxidation of **1**. Two clear isosbestic points are observed. The resulting spectrum displays a distinct absorption

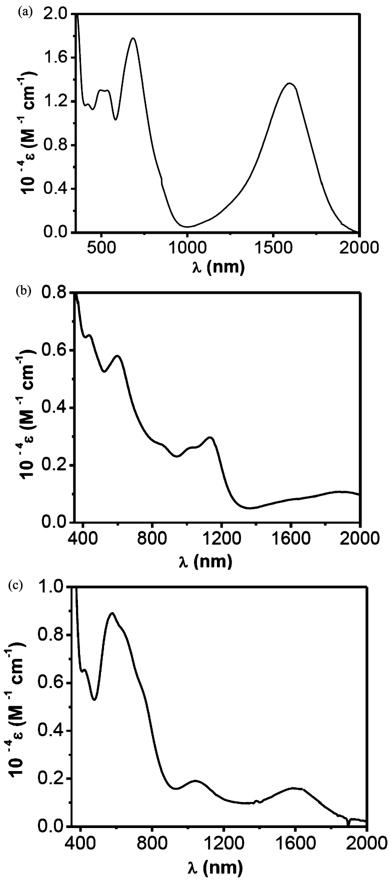

Figure 7. UV−vis−NIR spectra of (a) $[Fe^{III}(L)_2]$ **1**, (b) $[Fe^{III}(L)_2][BF_4]$ **2**, and (c) $[Co^{III}(\eta^5\text{-}C_{10}H_{15})_2][Fe^{III}(L)_2]$ **3** in CH_2Cl_2.

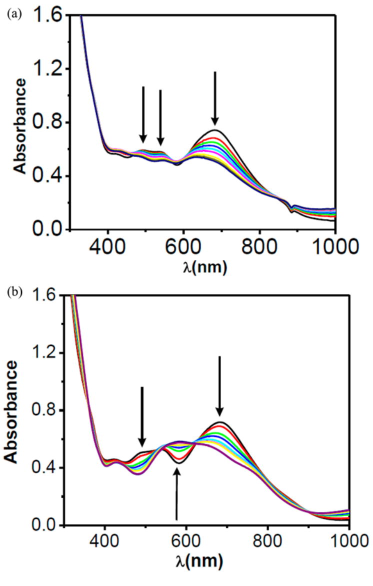

Figure 8. Changes in absorption spectral feature during spectroelectrochemical experiment: (a) coulometric oxidation at 0.7 V vs SCE and (b) coulometric reduction at −0.7 V vs SCE of a 1 mM solution (CH_2Cl_2 containing 0.1 M TBAP; 298 K) of $[Fe^{III}(L)_2]$ **1**.

maximum at 600 nm (see Absorption Spectra section). Electrochemical re-reduction of solutions of $[\mathbf{1}]^+$ produced quantitatively the spectrum of **1**. Figure 8b shows the absorption spectral changes during electrochemical one-electron reduction of **1**. During reduction two clear isosbestic points are observed. The resulting spectrum of $[\mathbf{1}]^-$ exhibits an absorption maximum at 570 nm and two shoulders at 650 and 755 nm (see Absorption Spectra section). Electrochemical reoxidation of solutions of $[\mathbf{1}]^+$ produced quantitatively **1**.

EPR Spectra. The diamagnetism of **1** indicates a strong intramolecular antiferromagnetic coupling between the $S_{\mathrm{Fe}} = 1/2$ spin of the LS $\mathrm{Fe^{III}}$ (see Mössbauer section) and the $S_{\mathrm{rad}} = 1/2$ spin distributed over two ligands (see X-ray and DFT section). Thus **1** is EPR silent. Isolated **2** in CH_2Cl_2 at 77 K exhibits an isotropic signal at $g = 2.002$ (Figure S12, Supporting Information). However, CH_2Cl_2-toluene glass (77 K) of **2** (Figure S12, Supporting Information) displays a sharp signal, with a slight anisotropy. From simulations of the latter spectra the following g values are obtained: $g_x = g_y = 2.003$, $g_z = 1.98$. Clearly, the signal corresponds to a ligand-based radical. The electronic structure of $[\mathbf{1}]^+/\mathbf{2}$ could then be assigned as $[\mathrm{Fe^{III}}\{(\mathrm{L^{ISQ}})^{-\bullet}\}_2]^+$ ($S = 1/2$ due to $(\mathrm{L^{ISQ}})^{-\bullet}$, considering antiferromagnetic coupling between a LS $\mathrm{Fe^{III}}$ center and a $(\mathrm{L^{ISQ}})^{-\bullet}$ radical; see X-ray, Mössbauer, and DFT section). Coulometrically generated (CH_2Cl_2, 0.1 M in TBAP) solutions of $[\mathbf{1}]^-$ at 77 K and also of **3** as CH_2Cl_2-toluene (1:1 v/v) glass at 77 K (Figure S13, Supporting Information) display rhombic EPR spectra, characterized by $S = 1/2$. From simulations the following g values are obtained: $g_x = 2.123$, $g_y = 2.007$, $g_z = 1.987$ ($g_{\mathrm{av}} = 2.039$). Notably, the g_{av} value of **3** is considerably lower than that of authentic six-coordinate LS $\mathrm{Fe^{III}}$ complexes[47] but is higher than that of $[\mathrm{M^{II}}\{(\mathrm{L^{ISQ}})^{-\bullet}\}(\mathrm{bpy})][\mathrm{PF_6}]$ (bpy = 2,2′-bipyridine; M = Pd and Pt).[38f] The latter complexes exhibit a $S = 1/2$ signal due to $(\mathrm{L^{ISQ}})^{-\bullet}$ at $g_{\mathrm{iso}} = 2.002$ for Pd and $g_{\mathrm{iso}} = 2.0$ for Pt. The unpaired electron in **3** thus predominantly resides in a metal d orbital (see DFT section). The electronic structure of $[\mathbf{1}]^-/\mathbf{3}$ could then be assigned as $[\mathrm{Fe^{III}}\{(\mathrm{L^{AP}})^{2-}\}_2]^-$. Thus the first one-electron oxidation and reduction of **1** are both ligand-centered processes, and the spin-state of $\mathrm{Fe^{III}}$ remains invariant.

To substantiate the phenomenon of valence-tautomerism (see Mössbauer and Absorption Spectra section) temperature-dependent EPR measurements were done on **2** and **3** at 298, 200, 120, and 77 K. At 298 K the signal ($g = 2.002$) of **2** as a solid is isotropic. As the temperature is lowered down to 120 K a noticeable asymmetry develops, however, without any measurable splitting (Figure 9). The spectra at 120 K (Figure 9) and 77 K (Figure S14, Supporting Information) are identical. In CH_2Cl_2-toluene (1:1; v/v) **2** exhibits at 298 and 200 K an isotropic signal; however, at 120 K the signal is clearly asymmetric (Figure 9). At 298 K complex **3** as polycrystalline solid is characterized by the g values 2.120, 2.061, 2.055 br, 2.012, and 1.990. On lowering temperature down to 200 and 120 K the feature at g values of 2.061 and 2.055 is clearly resolved, but the rest of the feature remains invariant (Figure 10a). At 77 K the spectrum is not well-resolved (Figure S14, Supporting Information). In CH_2Cl_2-toluene (1:1; v/v) **3** exhibits at 298 K an isotropic signal at $g = 2.048$. At 200 and 120 K the signal is clearly anisotropic with g values of 2.126, 2.064, 2.016, and 1.997 (Figure 10b). Notably, for **3** as glass (77 K) the signal at $g = 2.064$ is absent (Figure S13, Supporting Information). We assign the rhombic signal of **3** as CH_2Cl_2-toluene glass at 298, 200, and 120 K with g values of 2.126, 2.016, and 1.997 is due to $[\mathrm{Fe^{III}}\{(\mathrm{L^{AP}})^{2-}\}_2]^-$ and the signal at $g = 2.064$ as due to $[\mathrm{Fe^{II}}\{(\mathrm{L^{ISQ}})^{-\bullet}\}\{(\mathrm{L^{AP}})^{2-}\}]^-$ (LS $\mathrm{Fe^{II}}$). Solid of **3** behaves similarly. Temperature-dependent EPR spectral behavior of **2** and **3** clearly point toward thermally driven valence-tautomerism[2b,c,7a,10−12,42,50,51] (see Mössbauer and Absorption Spectra sections), for **3** at 77 K $[\mathrm{Fe^{III}}\{(\mathrm{L^{AP}})^{2-}\}_2]^-$ is favored and at higher temperatures $[\mathrm{Fe^{II}}\{(\mathrm{L^{ISQ}})^{-\bullet}\}\{(\mathrm{L^{AP}})^{2-}\}]^-$ is favored. We believe that intramolecular electron-exchange occurring on the EPR time scale contribute to the temperature dependence of the EPR spectra.

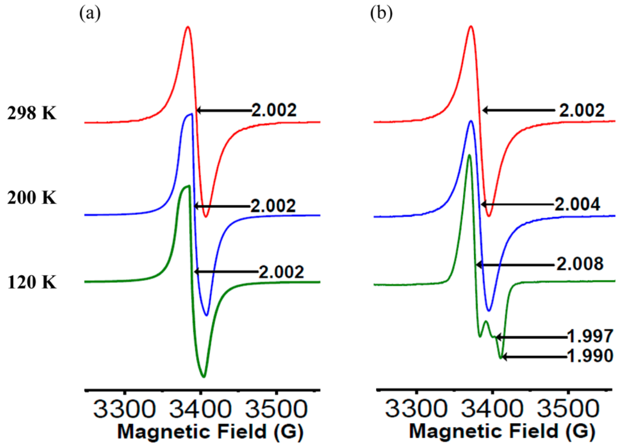

Figure 9. Temperature dependence of EPR spectra recorded for $[\mathrm{Fe^{III}}(\mathrm{L})_2][\mathrm{BF_4}]$ **2** (a) solid and (b) CH_2Cl_2-toluene (1:1; v/v).

DFT Calculations. Along with structural and spectroscopic investigation, theoretical calculations were also performed to understand the electronic structure of the neutral, monocationic, and monoanionic form of the complexes, that is, to make correct assignment of the redox level of the metal and the coordinated ligands in $[\mathbf{1}]$, $[\mathbf{1}]^+$, and $[\mathbf{1}]^-$. DFT-calculated at the B3LYP level (see Computational Details in the Experimental Section) bond parameters, based on the optimized structures of $[\mathbf{1}]$, $[\mathbf{1}]^+$, and $[\mathbf{1}]^-$ (Tables S1−S3, Supporting Information), match fairly well with the experimental data (Table 2 and Table S4, Supporting Information). DFT calculation for **1** leads to a broken-symmetry solution with one unpaired electron on the metal center and another one delocalized over two ligands.[52] One unpaired electron on iron implies that iron is present in the LS trivalent state. This is in accordance with the Mössbauer results. Since **1** is neutral three negative charges are expected to be contributed by the two ligands. This indicates that one ligand exists as dianionic form and the other one exists as a *o*-iminobenzosemiquinonate (1−) π radical. However, this unpaired electron (radical) is delocalized over both the ligands. The Mulliken spin-density plots and the spin-density values (Figure 11) revealed that the unpaired electron on LS $\mathrm{Fe^{III}}$ is antiferromagnetically coupled with the unpaired electron delocalized over both the ligands. The magnetic orbitals for **1** are displayed in Figure 12. The α-HOMO orbital has substantial ligand character (~86%) and the β-HOMO orbital is predominantly metal-centered (~73%). Strong spatial overlap ($S = 0.77$) between these orbitals accounts for its diamagnetism even at room temperature. Analysis of the LUMO orbitals shows that the α-LUMO orbital has ~95% ligand-character and is contributed by the $(\mathrm{L^{ISQ}})^{-\bullet}$ part of the ligand. Thus upon first reduction the electron is expected to be added to the *o*-iminobenzosemiquinonate(1−) part of the ligand to form *o*-amidophenolate(2−). The β-

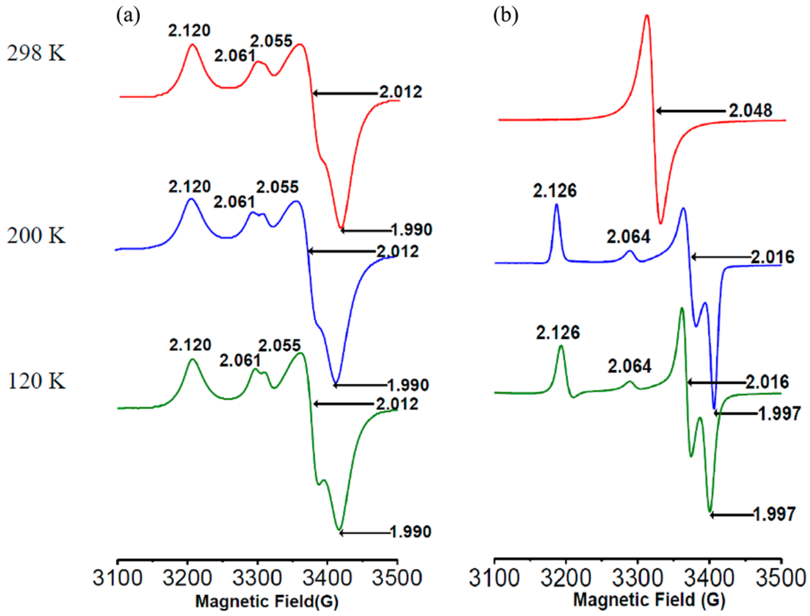

Figure 10. Temperature dependence of EPR spectra recorded for $[Co^{III}(\eta^5\text{-}C_{10}H_{15})_2][Fe^{III}(L)_2]$ **3** (a) solid and (b) CH_2Cl_2-toluene (1:1; v/v).

LUMO orbital is primarily ligand-based with ~32% metal-character. Notably, α-LUMO+1 and α-LUMO+2 orbitals are predominantly azo-based.

As revealed from the spin-density plot and spin-density values (Figure 11), upon oxidation the spin-population on the metal center in $[\mathbf{1}]^+$ remains unchanged. Thus oxidation takes place at the ligand center, and both the ligands exist in the $(L^{ISQ})^{-\bullet}$ level. The unpaired electron on the metal center couples antiferromagnetically with the unpaired electron on one of the ligands leading to $S = 1/2$ state. The singly occupied molecular orbital (SOMO) (Figure 12) has ~99% ligand-character which implies that the residual unpaired electron resides on the other ligand center. Analysis of the β-LUMO orbital reveals that it has ~99% primarily *o*-iminobenzosemiquinonate-based ligand character. Thus, during the course of $1e^-$ oxidation/reduction of $[\mathbf{1}]^+$ the $(L^{ISQ})^{-\bullet}$ will be responsible in the ligand redox level changes, while the metal center is not expected to undergo any change in its oxidation level.

DFT calculations suggest that $[\mathbf{1}]^-$ will have one unpaired electron. From the spin-density plot and the spin-density values (Figure 11) it is revealed that this electron resides on the metal center. So iron is in LS +3 oxidation state. Since the complex carries a negative charge and the metal ion is in the +3 oxidation state and there is no unpaired electron residing on the ligands, thus both the ligands exist in the $(L^{AP})^{2-}$ redox level. The SOMO (Figure 12) for $[\mathbf{1}]^-$ has predominantly metal-character (~66%).

TD-DFT Results. Time-Dependent (TD)-DFT calculations were done on **1**, $[\mathbf{1}]^+$, and $[\mathbf{1}]^-$ to get information about the origin of various absorptions occurring in the 400−2000 nm region and to get a trend within this series of complexes, varying in the oxidation level of the coordinated ligands but the oxidation state of the metal remaining invariant. The calculations on **1** revealed (Figure S15, Figure S16, and Table S5, Supporting Information) that the most allowed (f = 0.0786) lowest energy transition calculated at 1390 nm involves excitation from (α/β)-HOMO to (α/β)-LUMO. Inspection of frontier orbitals shows that this absorption in the near-IR region corresponds to a combination of ligand-to-ligand charge-transfer (LLCT) and ligand-to-metal charge-transfer (LMCT) transitions. The next absorptions calculated at lower wavelengths of 757 and 684 nm could be assigned as transitions from donor amidophenolate(2−) to the acceptor azo unit, along with minor metal-to-azo charge-transfer (MLCT) component, as revealed from the analysis of the frontier orbitals.

Upon oxidation the absorption(s) in the near-IR region is/are red-shifted and also the intensity decreased. TD-DFT (Figure S15, Figure S17, and Table S6, Supporting Information) results show that the near-IR spectral feature at 1636 nm corresponds to α-HOMO to α-LUMO transition with lower oscillator strength as compared to **1** (f = 0.0269 in $[\mathbf{1}]^+$ vs 0.0786 in **1**) than the lowest prominent excitation in **1**. The absorption at 1636 nm corresponds to LLCT and LMCT. The α-HOMO corresponds to electron density from the ligands scattered particularly on *o*-iminobenzosemiquinonate units while the α-LUMO has both metal and ligand contribution. Similar to what was observed for **1**, in the case of $[\mathbf{1}]^+$ also amidophenolate-to-azo charge-transfer (LLCT) and LMCT both occurs at lower wavelength region, calculated at 1181, 1072, and 682 nm. The orbitals involved in such transitions are β-HOMO and β-LUMO+2. Interestingly, we observe an excitation of minor contribution (~13%) at 682 nm from α-HOMO-1 to α-LUMO+1 orbital that is metal to ligand type, strengthening the existence of valence-tautomerism in $[\mathbf{1}]^+$ (cf. Mössbauer and EPR spectra).

For $[\mathbf{1}]^-$ the moderately allowed (f = 0.0236) lowest energy transition calculated by TD-DFT occurs at 1211 nm (Figure S15, Figure S18, and Table S7, Supporting Information). This excitation is amidophenolate-to-azo type. The next important transition occurs at 978 nm comprising the β-HOMO and β-LUMO+1 orbitals. Again similar excitations from both amidophenolate-to-azo (LLCT) and amidophenolate-to-metal (LMCT) were calculated. Additionally, metal-to-azo MLCT transition is calculated at 704 and 624 nm. As that for $[\mathbf{1}]^+$, the electronic transitions further substantiate the valence-tautomerism, prevalent in monoanion $[\mathbf{1}]^-$. Given the fact that absorption spectra of transition metal complexes is by far the

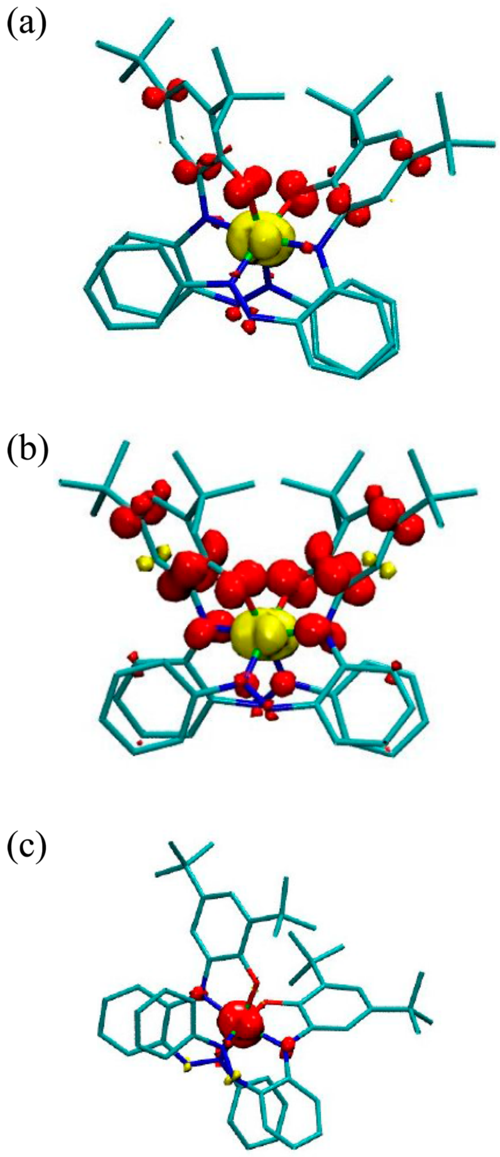

Figure 11. Spin-density plots of (a) $[Fe^{III}(L)_2]$ **1** (on each ligand 0.39 and on Fe^{III} −0.78), (b) $[\mathbf{1}]^+$ (on each ligand 0.89 and on Fe^{III} −0.80), and (c) $[\mathbf{1}]^-$ (on each ligand 0.037 and on Fe^{III} 0.93).

most difficult to calculate by DFT methods, we admit that the remarks made in this section on valence-tautomerism are highly speculative in nature.

■ SUMMARY AND CONCLUDING REMARKS

The most salient features of the present study are summarized here. A new complex $[Fe^{III}(L)_2]$ **1** coordinated by two tridentate redox-active azo-appended *o*-amidophenolate ligands has been synthesized. The monocation $[\mathbf{1}]^+$ – $[Fe^{III}(L)_2][BF_4]$ **2** – has been isolated and structurally, magnetically, and spectroscopically characterized. The monoanion $[\mathbf{1}]^-$ – $[Co^{III}(\eta^5\text{-}C_{10}H_{15})_2][Fe^{III}(L)_2]$ **3** – has also been isolated and magnetically and spectroscopically characterized. Structural analysis of **1** and **2**, room-temperature magnetic moment values of **2** and **3**, various spectroscopic data, and DFT calculations provide the spin-state of all three complexes. It has been conclusively deduced that the electronic structure of **1** must be described as a LS Fe^{III} stabilized by a ligand π radical delocalized over two ligands, providing together three negative charges. Strong intramolecular antiferromagnetic coupling between these two entities yields the observed diamagnetic (S = 0) ground state for **1**. The low-spin Fe^{III} in **2** is stabilized by two ligands each in the *o*-iminobenzosemiquinonate (1−) π radical $(L^{ISQ})^{-\bullet}$ form, and it is strongly antiferromagnetically coupled to one of the *o*-iminobenzosemiquinonato radicals (S_{rad} = 1/2), resulting in a doublet state due to other *o*-iminobenzosemiquinonato radical (S_{rad} = 1/2). The low-spin Fe^{III} in **3** is stabilized by two ligands each in the *o*-amidophenolate(2−) $(L^{AP})^{2-}$ form. It is demonstrated that the oxidation level of the coordinated ligands and LS state of Fe^{III} can be deduced by X-ray crystallographic metric parameters of reasonable quality in conjunction with ^1H NMR, mass, EPR, and Mössbauer, and UV−vis−NIR spectral data, and cyclic voltammetric results. We have provided evidence that valence-tautomerism is operative for **2** and **3**.

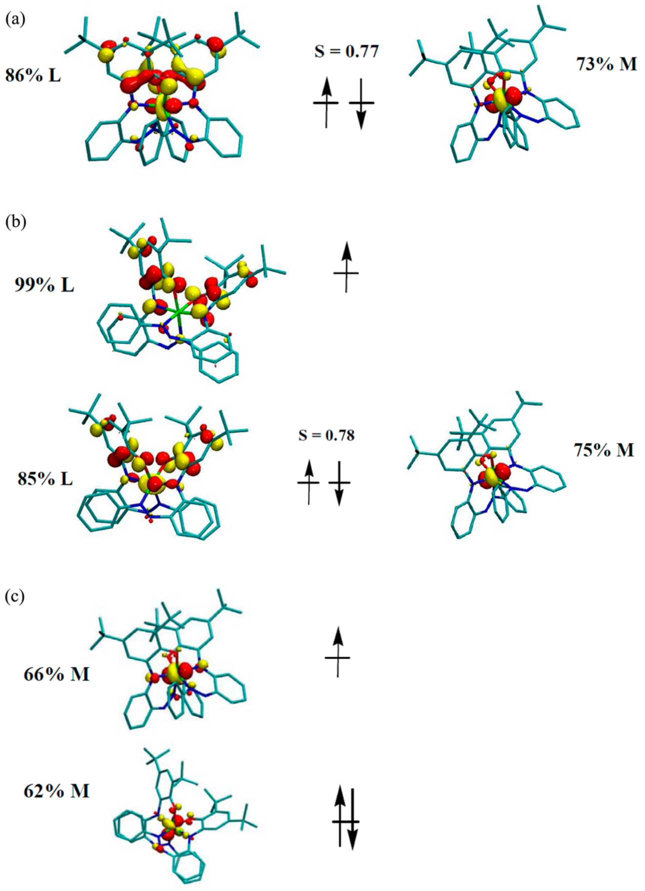

Figure 12. Qualitative MO diagrams of the magnetic orbitals for (a) $[Fe^{III}(L)_2]$ **1**, (b) $[\mathbf{1}]^+$, and (c) $[\mathbf{1}]^-$.

Exploration of the generality and versatility of the coordination behavior of this new tridentate ligand toward other transition metal ions is underway.

■ ASSOCIATED CONTENT

Ⓢ Supporting Information

^1H NMR spectra of H_2L and $[Fe^{III}(L)_2]$ **1** (Figures S1−S2); positive ESI−MS spectrum of $\{[Fe^{III}(L)_2] + H^+\}$ (Figure S3); CV scans of 1e$^-$ oxidized and 1e$^-$reduced solutions of $[Fe^{III}(L)_2]$ **1** in CH_2Cl_2 (Figures S4−S5, respectively); positive and negative ESI−MS spectra of $[Fe^{III}(L)_2][BF_4]$ **2** and $[Co^{III}(\eta^5\text{-}C_{10}H_{15})_2][Fe^{III}(L)_2]$ **3** (Figures S6−S7); Mössbauer spectra (solid) of **1** at 298 and 200 K (Figures S8); Mössbauer spectra (solid) of **1** at 80 K, **2** at 8 K, and **3** at 8 K (Figure S9); Mössbauer spectrum (solid) of **2** at 80 K (fitted three subspectra) (Figure S10); Mössbauer spectrum (solid) of **3** at 8 K (fitted two subspectra) (Figure S11); EPR spectra (77 K) of **2** in CH_2Cl_2 and in CH_2Cl_2-toluene glass (Figure S12); EPR spectra (77 K) of coulometrically generated $[\mathbf{1}]^-$ in CH_2Cl_2 and **3** in CH_2Cl_2-toluene glass (Figure S13); EPR spectra (77 K) of **2** and **3** as solid (Figure S14); TD-DFT-calculated electronic spectra of **1**, $[\mathbf{1}]^+$, and $[\mathbf{1}]^-$ (Figure S15); representative molecular orbitals involved in TD-DFT of **1**, $[\mathbf{1}]^+$, and $[\mathbf{1}]^-$ (Figures S16–S18, respectively); DFT-optimized Cartesian coordinates of **1**, $[\mathbf{1}]^+$, and $[\mathbf{1}]^-$ (Tables S1–S3, respectively); X-ray structural and DFT-optimized bond lengths of **1**, $[\mathbf{1}]^+$, and $[\mathbf{1}]^-$ (Tables S4); TD-DFT-calculated electronic transitions of **1**, $[\mathbf{1}]^+$, and $[\mathbf{1}]^-$ (Tables S5–S7, respectively). This material is available free of charge via the Internet at http://pubs.acs.org. CCDC-927552 (**1**) and 950999 (**2**) contain the supplementary crystallographic data for this paper. These data can be obtained free of charge from The Cambridge Crystallographic Data Centre via www.ccdc.cam.ac.uk/data_request/cif.

AUTHOR INFORMATION

Corresponding Author

*E-mail: rnm@iitk.ac.in. Phone: +91-512-2597437. Fax: +91-512-2597436.

Notes

The authors declare no competing financial interest.

ACKNOWLEDGMENTS

This work is supported by the Department of Science & Technology (DST), Government of India. R.M. sincerely thanks DST for a J.C. Bose fellowship. A.R. gratefully acknowledges the award of an SRF by UGC, and S.K.B. acknowledges the award of an SRF by the Council of Scientific & Industrial Research, Government of India. We are grateful to Dr. Serhiy Demeshko of Georg-August-Universität Göttingen for his help in temperature-dependent (200–8 K) Mössbauer spectral measurements. We sincerely thank Dr. Prasanta Ghosh of R. K. Mission Residential College, Narendrapur, Kolkata, for his help in temperature-dependent (298–120 K) EPR spectral measurements in his laboratory. Comments of the reviewers were very helpful at the revision stage.

REFERENCES

(1) (a) Jörgensen, C. K. *Coord. Chem. Rev.* **1966**, *1*, 164. (b) Jörgensen, C. K. In *Oxidation Numbers and Oxidation States*; Springer: Heidelberg, Germany, 1969. (c) Butin, K. P.; Beloglazkina, E. K.; Zyk, N. V. *Russ. Chem. Rev.* **2005**, *74*, 531–553.

(2) (a) Chirik, P. J. *Inorg. Chem.* **2011**, *50*, 9737–9740. (b) Kaim, W. *Inorg. Chem.* **2011**, *50*, 9752–9765. (c) Pierpont, C. G. *Inorg. Chem.* **2011**, *50*, 9766–9772. (d) Ray, K.; Petrenko, T.; Wieghardt, K.; Neese, F. *Dalton Trans.* **2007**, 1552–1566.

(3) (a) Stubbe, J. *Chem. Commun.* **2003**, 2511–2513. (b) Chaudhuri, P.; Wieghardt, K.; Weyhermüller, T.; Paine, T. K.; Mukherjee, S.; Mukherjee, C. *Biol. Chem.* **2005**, *386*, 1023–1033. (c) Thomas, F. *Eur. J. Inorg. Chem.* **2007**, 2379–2404. (d) Kaim, W.; Schwederski, B. *Coord. Chem. Rev.* **2010**, *254*, 1580–1588.

(4) Chirik, P. J.; Wieghardt, K. *Science* **2010**, *327*, 794–795.

(5) (a) Luca, O. R.; Crabtree, R. H. *Chem. Soc. Rev.* **2013**, *42*, 1440–1459. (b) Praneeth, V. K. K.; Ringenberg, M. R.; Ward, T. R. *Angew. Chem., Int. Ed.* **2012**, *51*, 10228–10234.

(6) King, E. R.; Betley, T. A. *J. Am. Chem. Soc.* **2009**, *131*, 14374–14380 and references therein.

(7) (a) Rall, J.; Wanner, M.; Albrecht, M.; Hornung, F. M.; Kaim, W. *Chem.—Eur. J.* **1999**, *5*, 2802–2809. (b) Khusniyarov, M. M.; Harms, K.; Burghaus, O.; Sundermeyer, J.; Sarkar, B.; Kaim, W.; van Slageren, J.; Duboc, C.; Fiedler, J. *Dalton Trans.* **2008**, 1355–1365.

(8) Pierpont, C. G.; Buchanan, R. M. *Coord. Chem. Rev.* **2001**, *38*, 45–87.

(9) Bill, E.; Bothe, E.; Chaudhuri, P.; Chlopek, K.; Herebian, D.; Kokatam, S.; Ray, K.; Weyhermüller, T.; Neese, F.; Wieghardt, K. *Chem.—Eur. J.* **2005**, *11*, 204–224 and references therein.

(10) (a) Shimazaki, Y.; Tani, F.; Fukui, K.; Naruta, Y.; Yamauchi, O. *J. Am. Chem. Soc.* **2003**, *125*, 10512–10513. (b) Shimazaki, Y.; Huth, S.; Karasawa, S.; Hirota, S.; Naruta, Y.; Yamauchi, O. *Inorg. Chem.* **2004**, *43*, 7816–7822. (c) Shimazaki, Y.; Yajima, T.; Tani, F.; Karasawa, S.; Fukui, K.; Naruta, Y.; Yamauchi, O. *J. Am. Chem. Soc.* **2007**, *129*, 2559–2568.

(11) (a) Rotthaus, O.; Jarjayes, O.; Thomas, F.; Philouze, C.; Valle, C. P. D.; Saint-Aman, E.; Pierre, J.-L. *Chem.—Eur. J.* **2006**, *12*, 2293–2302. (b) Rotthaus, O.; Thomas, F.; Jarjayes, O.; Philouze, C.; Saint-Aman, E.; Pierre, J.-L. *Chem.—Eur. J.* **2006**, *12*, 6953–6962. (c) Rotthaus, O.; Jarjayes, O.; Valle, C. P. D.; Philouze, C.; Thomas, F. *Chem. Commun.* **2007**, 4462–4464. (d) Rotthaus, O.; Labet, V.; Philouze, C.; Jarjayes, O.; Thomas, F. *Eur. J. Inorg. Chem.* **2008**, 4215–4224. (e) Rotthaus, O.; Jarjayes, O.; Philouze, C.; Valle, C. P. D.; Thomas, F. *Dalton Trans.* **2009**, 1792–1800. (f) Orio, M.; Jarjayes, O.; Kanso, H.; Philouze, C.; Neese, F.; Thomas, F. *Angew. Chem., Int. Ed.* **2010**, *49*, 4989–4992.

(12) (a) Storr, T.; Wasinger, E. C.; Pratt, R. C.; Stack, T. D. P. *Angew. Chem., Int. Ed.* **2007**, *46*, 5198–5201. (b) Storr, T.; Verma, P.; Pratt, R. C.; Wasinger, E. C.; Shimazaki, Y.; Stack, T. D. P. *J. Am. Chem. Soc.* **2008**, *130*, 15448–15459. (c) Storr, T.; Verma, P.; Shimazaki, Y.; Wasinger, E. C.; Stack, T. D. P. *Chem.—Eur. J.* **2010**, *16*, 8980–8983.

(13) (a) Joy, S.; Pal, P.; Mondal, T. K.; Talapatra, G. B.; Goswami, S. *Chem.—Eur. J.* **2012**, *18*, 1761–1771. (b) Samanta, S.; Ghosh, P.; Goswami, S. *Dalton Trans.* **2012**, *41*, 2213–2226. (c) Paul, N. D.; Rana, U.; Goswami, S.; Mondal, T. K.; Goswami, S. *J. Am. Chem. Soc.* **2012**, *134*, 6520–6523.

(14) Poddel'sky, A. I.; Cherkasov, V. K.; Abakumov, G. A. *Coord. Chem. Rev.* **2009**, *253*, 291–324.

(15) (a) Mukherjee, A.; Lloret, F.; Mukherjee, R. *Inorg. Chem.* **2008**, *47*, 4471–4480. (b) Mukherjee, A.; Lloret, F.; Mukherjee, R. *Eur. J. Inorg. Chem.* **2010**, 1032–1042. (c) Mukherjee, A.; Mukherjee, R. *Indian J. Chem.* **2011**, *50A*, 484–490 and references therein.

(16) Najafpour, J.; Foroutan-Nejad, C.; Shafiee, G. H.; Peykani, M. K. *Comput. Theor. Chem.* **2011**, *974*, 86–91 and references therein.

(17) (a) Noro, S.-i.; Chang, H.-C.; Takenobu, T.; Murayama, Y.; Kanbara, T.; Aoyama, T.; Sassa, T.; Wada, T.; Tanaka, D.; Kitagawa, S.; Iwasa, Y.; Akutagawa, T.; Nakamura, T. *J. Am. Chem. Soc.* **2005**, *127*, 10012–10013. (b) Wickramasinghe, L. D.; Perera, M. M.; Li, L.; Mao, G.; Zhou, Z.; Verani, C. N. *Angew. Chem., Int. Ed.* **2013**, DOI: 10.1002/anie.201306765.

(18) Chen, J.; Lee, T.; Su, J.; Wang, W.; Reed, M. A.; Rawlett, A. M.; Kozaki, M.; Yao, Y.; Jagessar, R. C.; Dirk, S. M.; Price, D. W.; Tour, J. M.; Grubisha, D. S.; Bennett, D. W. On Molecular Electronic Devices. In *Molecular Nanoelectronics*; Reed, M. A., Lee, T., Eds.; American Scientific Publishers: Stevenson Ranch, CA , **2003**; pp. 1–76.

(19) Deibel, N.; Schweinfurth, D.; Hohloch, S.; Fiedler, J.; Sarkar, B. *Chem. Commun.* **2012**, *48*, 2388–2390.

(20) (a) Pandey, S. P.; Das, P. P.; Singh, A. K.; Mukherjee, R. *Dalton Trans.* **2011**, *40*, 10758–10768. (b) Sharma, A. K.; Biswas, S.; Barman, S. K.; Mukherjee, R. *Inorg. Chim. Acta* **2010**, *363*, 2720–2727.

(21) Kaiya, T.; Fujiwara, T.; Kohda, K. *Chem. Res. Toxicol.* **2000**, *13*, 993–1001.

(22) Chaudhuri, M. K.; Ghosh, S. K. *J. Chem. Soc., Dalton Trans.* **1983**, 839–840.

(23) Ray, M.; Mukerjee, S.; Mukherjee, R. *J. Chem. Soc., Dalton Trans.* **1990**, *36*, 3635–3638.

(24) Mukherjee, R.; Pulla Rao, C.; Holm, R. H. *Inorg. Chem.* **1986**, *25*, 2979–2989.

(25) (a) Ray, M.; Ghosh, D.; Shirin, Z.; Mukherjee, R. *Inorg. Chem.* **1997**, *36*, 3568−3572. (b) Patra, A. K.; Mukherjee, R. *Inorg. Chem.* **1999**, *38*, 1388−1393. (c) Singh, A. K.; Balamurugan, V.; Mukherjee, R. *Inorg. Chem.* **2003**, *42*, 6497−6502.

(26) O'Connor, C. J. *Prog. Inorg. Chem.* **1982**, *29*, 203−283.

(27) Evans, D. F. *J. Chem. Soc.* **1959**, 2003−2005.

(28) Albers, A.; Demeshko, S.; Pröpper, K.; Dechert, S.; Bill, E.; Meyer, F. *J. Am. Chem. Soc.* **2013**, *135*, 1704−1707.

(29) Farrugia, L. J. *WinGX version 1.64, An Integrated Systems of Windows Programs for the Solution, Refinement and Analysis of Single-Crystal X-ray Diffraction Data*; Department of Chemistry, University of Glasgow: Glasgow, U.K., 2003.

(30) Frisch, M. J.; Trucks, G. W.; Schlegel, H. B.; Scuseria, G. E.; Robb, M. A.; Cheeseman, J. R.; Scalmani, G.; Barone, V.; Mennucci, B.; Petersson, G. A.; Nakatsuji, H.; Caricato, M.; Li, X.; Hratchian, H. P.; Izmaylov, A. F.; Bloino, J.; Zheng, G.; Sonnenberg, J. L.; Hada, M.; Ehara, M.; Toyota, K.; Fukuda, R.; Hasegawa, J.; Ishida, M.; Nakajima, T.; Honda, Y.; Kitao, O.; Nakai, H.; Vreven, T.; Montgomery, J. A., Jr.; Peralta, J. E.; Ogliaro, F.; Bearpark, M.; Heyd, J. J.; Brothers, E.; Kudin, K. N.; Staroverov, V. N.; Kobayashi, R.; Normand, J.; Raghavachari, K.; Rendell, A.; Burant, J. C.; Iyengar, S. S.; Tomasi, J.; Cossi, M.; Rega, N.; Millam, N. J.; Klene, M.; Knox, J. E.; Cross, J. B.; Bakken, V.; Adamo, C.; Jaramillo, J.; Gomperts, R.; Stratmann, R. E.; Yazyev, O.; Austin, A. J.; Cammi, R.; Pomelli, C.; Ochterski, J. W.; Martin, R. L.; Morokuma, K.; Zakrzewski, V. G.; Voth, G. A.; Salvador, P.; Dannenberg, J. J.; Dapprich, S.; Daniels, A. D.; Farkas, Ö.; Foresman, J. B.; Ortiz, J. V.; Cioslowski, J.; Fox, D. J. *Gaussian 09*, revision C.01; Gaussian, Inc.: Wallingford, CT, 2010.

(31) (a) Becke, A. D. *J. Chem. Phys.* **1993**, *98*, 5648−5652. (b) Lee, C.; Yang, W.; Parr, R. G. *Phys. Rev. B* **1988**, *37*, 785−789. (c) Stevens, P. J.; Devlin, F. J.; Chabalowski, C. F.; Frisch, M. *J. Phys. Chem.* **1994**, *98*, 11623−11627.

(32) Schafer, A.; Horn, H.; Ahlrichs, R. *J. Chem. Phys.* **1992**, *97*, 2571−2577.

(33) Schafer, A.; Huber, C.; Ahlrichs, R. *J. Chem. Phys.* **1994**, *100*, 5829−5835.

(34) Bachler, V.; Olbrich, G.; Neese, F.; Wieghardt, K. *Inorg. Chem.* **2002**, *41*, 4179−4193.

(35) (a) Humphrey, W.; Dalke, A.; Schulten, K. *J. Mol. Graphics* **1996**, *14*, 33−38. (b) http://www.chemcraftprog.com/

(36) (a) Barone, V.; Cossi, M. *J. Phys. Chem. A* **1998**, *102*, 1995−2001. (b) Cossi, M.; Barone, V. *J. Chem. Phys.* **2001**, *115*, 4708−4717. (c) Cossi, M.; Rega, N.; Scalmani, G.; Barone, V. *J. Comput. Chem.* **2003**, *24*, 669−681.

(37) O'Boyle, N. M.; Tenderholt, A. L.; Langner, K. M. *J. Comput. Chem.* **2008**, *29*, 839−845.

(38) (a) Chaudhuri, P.; Verani, C. N.; Bill, E.; Bothe, E.; Weyhermüller, T.; Wieghardt, K. *J. Am. Chem. Soc.* **2001**, *123*, 2213−2223. (b) Chun, H.; Verani, C.; Chaudhuri, P.; Bothe, E.; Bill, E.; Weyhermüller, T.; Wieghardt, K. *Inorg. Chem.* **2001**, *40*, 4157−4166. (c) Chun, H.; Chaudhuri, P.; Weyhermüller, T.; Wieghardt, K. *Inorg. Chem.* **2002**, *41*, 790−795. (d) Herebian, D.; Ghosh, P.; Chun, H.; Bothe, E.; Weyhermüller, T.; Wieghardt, K. *Eur. J. Inorg. Chem.* **2002**, 1957−1967. (e) Bachler, V.; Olbrich, G.; Neese, F.; Wieghardt, K. *Inorg. Chem.* **2002**, *41*, 4179−4193. (f) Sun, X.; Chun, H.; Hildenbrand, K.; Bothe, E.; Weyhermüller, T.; Neese, F.; Wieghardt, K. *Inorg. Chem.* **2002**, *41*, 4295−4303. (g) Min, K. S.; Weyhermüller, T.; Wieghardt, K. *Dalton Trans.* **2003**, 1126−1132. (h) Min, K. S.; Weyhermüller, T.; Bothe, E.; Wieghardt, K. *Inorg. Chem.* **2004**, *43*, 2922−2931. (i) Bill, E.; Bothe, E.; Chaudhuri, P.; Chlopek, K.; Herebian, D.; Kokatam, S.; Ray, K.; Weyhermüller, T.; Neese, F.; Wieghardt, K. *Chem.—Eur. J.* **2005**, *11*, 204−224. (j) Mukherjee, S.; Weyhermüller, T.; Bill, E.; Wieghardt, K.; Chaudhuri, P. *Inorg. Chem.* **2005**, *44*, 7099−7108.

(39) Saha Roy, A.; Saha, P.; Das Adhikary, N.; Ghosh, P. *Inorg. Chem.* **2011**, *50*, 2488−2500.

(40) Ye, S.; Sarkar, B.; Lissner, F.; Schleid, T.; van Slageren, J.; Fiedler, J.; Kaim, W. *Angew. Chem., Int. Ed.* **2005**, *44*, 2103−2106.

(41) (a) Das, D.; Mondal, T. K.; Dutta Chowdhury, A.; Weisser, F.; Schweinfurth, D.; Sarkar, B.; Mobin, S. M.; Urbanos, F. A.; Jiménez-Aparicio, R.; Lahiri, G. K. *Dalton Trans.* **2011**, *40*, 8377−8390 and refs therein. (b) Das, D.; Agarwala, H.; Dutta Chowdhury, A.; Patra, T.; Mobin, S. M.; Sarkar, B.; Kaim, W.; Lahiri, G. K. *Chem.—Eur. J.* **2013**, *19*, 7383−7394.

(42) Kokatam, S.; Weyhermüller, T.; Bothe, E.; Chaudhuri, P.; Wieghardt, K. *Inorg. Chem.* **2005**, *44*, 3709−3717.

(43) Connelly, N. G.; Geiger, W. E. *Chem. Rev.* **1996**, *96*, 877−910.

(44) Calderazzo, F.; Pampaloni, G.; Englert, U. *J. Organomet. Chem.* **1990**, *383*, 45−57.

(45) Saha, A.; Majumdar, P.; Peng, S.-M.; Goswami, S. *Eur. J. Inorg. Chem.* **2000**, 2631−2639.

(46) Paul, N.; Samanta, S.; Goswami, S. *Inorg. Chem.* **2010**, *49*, 2649−2655.

(47) (a) Patra, A. K.; Ray, M.; Mukherjee, R. *Inorg. Chem.* **2000**, *39*, 652−657. (b) Ray, M.; Mukherjee, R.; Richardson, J. F.; Buchanan, R. M. *J. Chem. Soc., Dalton Trans.* **1993**, 2451−2457.

(48) Mishra, V.; Mukherjee, R.; Linares, J.; Balde, C.; Desplanches, C.; Létard, J.-F.; Collet, E.; Toupet, L.; Castro, M.; Varret, F. *Inorg. Chem.* **2008**, *47*, 7577−7587.

(49) Chun, H.; Bill, E.; Bothe, E.; Weyhermüller, T.; Wieghardt, K. *Inorg. Chem.* **2002**, *41*, 5091−5099.

(50) (a) Pierpont, C. G. *Coord. Chem. Rev.* **2001**, *216−217*, 99−125. (b) Hendrickson, D. N.; Pierpont, C. G. *Top. Curr. Chem.* **2004**, *234*, 63−95.

(51) Minkin, V. I.; Starikova, A. A.; Minyaev, R. M. *Dalton Trans.* **2013**, *42*, 1726−1734.

(52) Kapre, R. R.; Bothe, E.; Weyhermüer, T.; DeBeer George, S.; Muresan, N.; Wieghardt, K. *Inorg. Chem.* **2007**, *46*, 7827−7839.